Ultra-fast high-temperature sintering (UHS) of Ce0.2Zr0.2Y0.2Gd0.2La0.2O2- fluorite-structured entropy-stabilized oxide (F-ESO)

(Article begins on next page)

24 April 2024

Ultra-fast High-temperature Sintering (UHS) of Ce$_{0.2}$Zr$_{0.2}$Y$_{0.2}$Gd$_{0.2}$La$_{0.2}$O$_{2-\delta}$ Fluorite-structured Entropy-Stabilized Oxide (F-ESO)

Luca Spiridigliozzi[1,*], Gianfranco Dell'Agli[1,2], Serena Esposito[2,3], Paola Rivolo[3], Salvatore Grasso[4], Vincenzo M. Sglavo[2,5], Mattia Biesuz[5,*]

[1] Department of Civil and Mechanical Engineering, University of Cassino and Southern Lazio, Via G. Di Biasio 43, 03043 Cassino (FR), Italy;

[2] INSTM—National Interuniversity Consortium of Materials Science and Technology, Via G. Giusti 9, 50121 Florence, Italy;

[3] Department of Applied Science and Technology, Politecnico di Torino, Corso Duca degli Abruzzi 24, Torino I-10129, Italy;

[4] Key Laboratory of Advanced Technologies of Materials, Ministry of Education, School of Materials Science and Engineering, Southwest Jiaotong, Chengdu 610031, China;

[5] Department of Industrial Engineering, Via Sommarive 9, 38123 Trento, Italy;

[*] Corresponding author: l.spiridigliozzi@unicas.it (Luca Spiridigliozzi);

mattia.biesuz@unitn.it (Mattia Biesuz).

Abstract

Single-phase high entropy fluorite (Ce$_{0.2}$Zr$_{0.2}$Y$_{0.2}$Gd$_{0.2}$La$_{0.2}$O$_{2-\delta}$) samples were synthesized by co-precipitation and consolidated by ultrafast high-temperature sintering (UHS) in less than 2 min. The chemical homogeneity of the sintered materials was confirmed by X-Ray Diffraction (XRD), Energy Dispersive X-ray Spectroscopy (EDXS), high-resolution EDXS in Transmission Electron Microscopy (TEM), and Raman spectroscopy. Compared to conventional sintering, UHS of high entropy ceramics was a hundred times faster and it resulted in extremely dense microstructures (relative density > 93%) with nanometric grains. Ce$_{0.2}$Zr$_{0.2}$Y$_{0.2}$Gd$_{0.2}$La$_{0.2}$O$_{2-\delta}$ densifies when the UHS current passes from 20 to 25 A. On these bases, an optimized step-wise UHS schedule was developed to get dense, single-phase pellets with a reduced amount of defects. The extreme heating rates appear beneficial both for microstructural and phase evolution.

Keywords: ultrafast high-temperature sintering; UHS; high entropy oxides; fluorite; co-precipitation

Main Body

Processing materials from powders into dense bodies at high temperature is commonly known as sintering and dates back to the Paleolithic age [1]. It is a highly energy-consuming process as it requires long dwell time (some hours) at a very high temperature to promote diffusion and reach full densification. In recent years, novel sintering routes have been developed to reduce the carbon footprint of the ceramic industry, many of them involving high heating rate processes such as spark plasma sintering [2,3], microwave sintering [4,5], flash sintering [6-8], fast-firing [9,10] and, more recently, ultrafast high-temperature sintering (UHS) [11]. Among these techniques, UHS is ~~of particular interest~~ particularly interesting as it allows reaching very high temperatures (>2000°C) [12,13] within a few seconds/minutes ~~while allowing to~~ and processing samples with complex shapes [11] and different electrical/dielectric properties [11–18]. A typical UHS setup includes a carbon felt strip in an inert atmosphere, within which the green body is positioned and heated by the Joule energy developed by an electric current passing through the felt, whose low thermal inertia guarantees very fast heating/cooling.

Other strategies aiming at reducing the sintering temperature involved the development of highly sinterable nanopowder, the sintering rates being inversely proportional to a power law of the grain size [19]. In addition, by applying fast heating to ceramic nanopowder, it is possible to obtain fully dense materials [20] with fine-grained microstructure and, consequently, novel mechanical/functional properties.

Entropy-Stabilized Oxides (ESO) are a new class of materials introduced by Rost et al. in 2015 [21], who demonstrated the configurational entropy stabilization of a 5-component oxide $(Mg_{0.2}Co_{0.2}Ni_{0.2}Zn_{0.2}Cu_{0.2})O$. Following Rost's work, many other multicomponent oxide systems have been proven to be entropy-stabilized [22–32] and characterized by unexpected and fascinating properties [33–44].

High entropy fluorites are of particular interest because of the presence of several cations in solid solution which allows tuning their thermal conductivity [45], ~~which is~~ being of pivotal importance in applications like thermal barrier coatings. Nevertheless, these materials are relatively difficult to be manufactured by solid-state synthesis (i.e., annealing of mono-element oxide powders) and sintering, this requiring temperature as high as 1800°C [30] or extremely prolonged dwell time (10 h) at lower temperatures (1400°C) [45]. Therefore, they represent an ideal system to validate the effectiveness of UHS to produce single-phase multielement ceramics.

In the present work, we investigated the feasibility of UHS to obtain dense $Ce_{0.2}Zr_{0.2}Y_{0.2}Gd_{0.2}La_{0.2}O_{2-\delta}$ samples using nanopowder synthesized by co-precipitation. The composition was selected ~~following~~ according to a previous study [46] ~~which confirmed~~ confirming that the system is entropy stabilized (this means that the multi-phase to single-phase transition is reversible upon cooling).

Ce(NH$_4$)$_2$(NO$_3$)$_6$, ZrO(NO$_3$)$_2$ (Carlo Erba, Milan, Italy), and Y(NO$_3$)$_3$·6H$_2$O, Gd(NO$_3$)$_3$·6H$_2$O, La(NO$_3$)$_3$·6H$_2$O (Sigma Aldrich, Milan, Italy) were used as metal precursors for the synthesis of Ce$_{0.2}$Zr$_{0.2}$Y$_{0.2}$Gd$_{0.2}$La$_{0.2}$O$_{2-\delta}$, while ammonium carbonate (J.T. Baker, The Netherlands) was used as precipitating agent. The whole synthesis process, based on the optimization of the co-precipitation step, was transposed from a previous work [8] where the detailed procedure is described; the only difference is in the use of 0.5 M ammonium carbonate solution (whose volume is fixed by the molar ratio carbonate/total metal = 2.5) instead of diluted ammonia solution as precipitating agent. Bearing in mind the thermal behavior of the as-synthesized Ce$_{0.2}$Zr$_{0.2}$Y$_{0.2}$Gd$_{0.2}$La$_{0.2}$O$_{2-\delta}$, characterized by a two-step complete decomposition completed at about 700°C (**Figure S1**), these powders were calcined at 750°C for 1 h to allow the embodied water and CO$_2$ evolution.

The calcined powder (0.2 g) was uniaxial pressed under 150 MPa (diameter = 8 mm) and then sintered both conventionally at 1550 °C (heating rate = 10°C min^{-1}) for 2 h (followed by cooling at 20°C min^{-1}) and via UHS using different conditions (**Table 1**). UHS was carried out in an Ar-filled borosilicate glass flask using graphite felt (SGL carbon Co., Germany) connected by means of copper wires to a Sorensen XG6025 power source. The felt cross-section was 6.5 x 29.5 mm, the electrode span was 33 mm. The green sample was introduced in the center of the felt within a small incision produced by cutting the center of the felt parallel to the current flow by a razor blade.

The sintering shrinkage of the green body during conventional heating cycle (10°C min^{-1} up to 1550°C) was quantified using a horizontal alumina dilatometer Linseis L75.

X-Ray Diffraction (XRD) patterns were obtained on an X'Pert Phillips diffractometer equipped with a PIXcel 1D detector operating at 40 kV and 40 mA with Cu Kα radiation (scanning resolution 2θ = 0.026°, time per step: 2 s) on the sintered samples.

The relative density was estimated as the ratio between the density measured by the Archimedes' method and the theoretical one, estimated according to the following general crystallographic correlation:

$$\rho = \frac{\sum_i \ n_i \, M_i}{a^3 \, N_A} \qquad (1)$$

where n_i is the number of atoms i in the unit cell, M_i the molar mass in g mol^{-1} of the element i, a the lattice parameter (determined by XRD) and N_A the Avogadro number.
SEM micrographs were taken on fresh fracture surfaces using a field-emission scanning electron microscope (SUPRA 4, Carl Zeiss Microscopy GmbH). The chemical analysis by electron-dispersive X-ray spectroscopy (EDXS) was carried out using a Jeol IT300 SEM equipped with XFlash 630 M detector (Bruker Quantax). Before SEM analysis, the samples were made conductive by sputtering a thin carbon layer.

Raman spectra were acquired with an In-Via Reflex micro-Raman spectrometer (Renishaw plc, Wotton-under-Edge, UK) equipped with a cooled CCD camera and a 785 nm laser source. A 50x objective was used to collect the spectra in backscattering configuration, by mapping the pelletized samples surface on a region of 100 µm x 80 µm with a step size of 20 µm (~20 spectra). The following conditions were employed to collect the spectral maps of Conv_1550 and UHS_5 sintered samples: 0.5 mW and 5 mW laser power,1 s exposure time and 10 accumulations. Average spectra calculation and baseline subtraction were performed using Wire 5.1 software.

The optimized UHS sample was observed by transmission electron microscope (TEM) to confirm the solid solution homogeneity. Since the ion milling process to obtain a TEM ultrathin section resulted quite challenging ~~after a few trials~~, the sample was milled in an agate mortar to produce thin powder. The obtained powder was placed on a C-coated Cu grid and analyzed using Thermofisher TALOS F200S equipment in bright field mode. Energy Dispersion X-ray Spectroscopy (EDXS) maps were acquired in scanning transmission electron microscope (STEM) mode.

Table 1. Labeling of the $Ce_{0.2}Zr_{0.2}Y_{0.2}Gd_{0.2}La_{0.2}O_{2-\delta}$ samples sintered using different conditions.

Labeling	Sintering method	Sintering/UHS conditions
Conv_1550	Conventional	1550 °C (heating rate 10 °C min^{-1}, cooling rate 20 °C min^{-1})
UHS_0	UHS	25 A, 60 s
UHS_1	UHS	10A 20s + 15A 20s + 20A 20s
UHS_2	UHS	10A 20s + 15A 20s + 20A 20s + 25A 10s
UHS_3	UHS	10A 20s + 15A 20s + 20A 20s + 25A 20s
UHS_4	UHS	10A 20s + 15A 20s + 20A 20s + 25A 60s
UHS_5	UHS	10A 20s + 15A 20s + 20A 20s + 22A 20s + 23.5A 20 s + 25A 20s

The sintering behavior of the calcined powder is shown in **Figure 1**. The onset sintering temperature (determined by tangent method) is ≈ 1180°C, whereas the maximum sintering rate is achieved at ≈ 1330°C. At 1550°C the material continues to shrink although the linear shrinkage is already ≈ 30%.
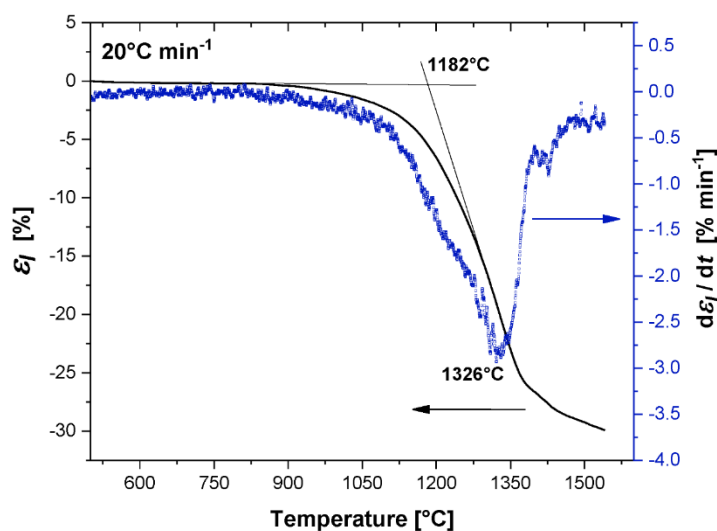
Figure 1. Linear sintering strain (ε_l) and its derivative as a function of temperature.

The relative density of the different UHS samples is reported in **Table 2**. ~~We can observe that~~ Treatments under 25 A (UHS_0, 2, 3, 4, and 5) always led to well-densified microstructure (relative density exceeding 93%), regardless of the processing time (10, 20, or 60 s). On the other hand, the sample treated under 20 A for 20 s (UHS_1) remained in an "almost green state", with final density below 70%, this pointing out that only the early sintering stages occurred. On these bases, it can be concluded ~~we can conclude~~ that most of the sintering process takes place when the current increases from 20 A to 25 A. As such, UHS cycles quickly crossing this relatively "narrow" current interval (UHS_0, 2, 3, and 4) caused the development of large defects and cracks, regardless of the current schedule up to 20 A. In fact, large flaws were detected in samples UHS_0 and UHS_2, 3, 4 where the former was directly heated under 25 A and the others were treated using a 5 A-step schedule. The absence of any crack in sample UHS_1 (20 A) further confirms that the "critical" current interval lies ~~is~~ between 20 and 25 A, i.e. where differential sintering strains can arise due to the surface/core thermal gradients. ~~On this basis~~ Accordingly, an optimized sintering schedule was developed by progressively increasing the current between 20 and 25 A (UHS_5), this procedure allowing to obtain almost defect-free components. Thus ~~This points out that~~, when dealing with UHS, in order to lower the thermal stresses and to obtain well-sintered and defect-free pellets, a particular care to define a properly "slow" current schedule in the temperature interval where sintering occurs should be taken, whereas the heating schedule up to such temperatures has a lesser impact on such characteristics ~~can be "as quick" as you want~~.

To compare the UHS temperatures with the conventional sintering ones, some metals ($\approx$ 20-40 mg) not reacting with carbon were introduced within the felts to check whether or not they melted during UHS (**Table 1**). Copper (T_m = 1085 °C) was melted in all cases, thus pointing out that 20 A for 20 s (UHS1) is sufficient to reach temperatures of $\approx$ 1100°C. To understand "how close"

5

was sample UHS1 to the melting point of copper, we carried out an additional test at 20 A for 15 s, which did not result in Cu melting. This suggests that the temperature reached during UHS_1 is relatively close to the melting point of copper. The conclusion seems quite consistent with the dilatometric plot (**Figure 1**) and the density measurement (**Table 1**), the sample UHS_1 remaining in the early sintering stages, and also with diffraction data as discussed below.

High purity nickel (T_m=1455°C) melted when 25 A were applied for a dwell time ranging between 10 and 20 s. In other words, the UHS_2 cycle remained below 1455°C whereas UHS_3 exceeded such temperature. It appears quite "surprising" that the UHS_2 sample, whose relative density exceeds 93%, remained well below 1500°C with a dwell time of only 10 s (at such temperature the sintering shrinkage is still not completed upon conventional heating). Although the uncertainty of the temperature estimation remains quite wide and the temperatures are not very far from those leading to full densification, these results suggest that the fast heating procedures of the $Ce_{0.2}Zr_{0.2}Y_{0.2}Gd_{0.2}La_{0.2}O_{2-\delta}$ nanopowder upon UHS has some beneficial effect on sintering. ~~One can observe that~~ Thus, it seems very unlikely that sample UHS_2 could have exceeded the melting point of Ni (T_m = 1455°C) since the thermal inertia of the ceramic sample is expected to be much larger than that of the metallic ones (whose weight is less than 1/5 with respect to the ceramics). Similar heating rates effects on sintering have been observed also in other fast-heating processes like fast-firing [9,10] and flash sintering [47,48]. Finally, melting of Pt (T_m = 1768 °C) did not occur even in severe conditions (UHS_0 and 4).

The excellent level of densification of the sample treated with the optimized UHS cycle (i.e., UHS_5) is confirmed by the SEM micrographs in **Figure 2**. The microstructure appears nearly fully dense with small amounts of tiny polygonal pores located at the grain boundaries. The fracture mechanism is intergranular and points out the formation of polygonal grains with sharp grain boundaries as fingerprints of an effective sintering process. Furthermore, the grain size appears well-submicrometric with modest differences between the sample surface and interior; such data well agree with the crystal size calculated by the Scherrer formula on the (220) reflection and which is equal to 347 nm. On the other hand, the sample sintered under conventional conditions results in an exaggerated grain coarsening with grains exceeding 10 μm.

Therefore, UHS, similarly to other rapid sintering technologies [6,49], stands as an effective route for achieving high densification levels while maintaining a fine-grained microstructure.

Table 2. The density of the sintered samples, presence of crack, and temperature estimation

Sample	Relative density [%]	Cracks	Temperature estimation		
			Cu (T_m=1085°C)	Ni (T_m=1455°C)	Pt (T_m=1768°C)
Conv_1550	99.1	Marginal on the edge			-

UHS_0	93.4	Abundant	Melted	Melted	Not Melted
UHS_1	67.7	None	Melted	Not Melted	Not Melted
UHS_2	93.7	Abundant	Melted	Not Melted	Not Melted
UHS_3	93.1	Abundant	Melted	Melted	Not Melted
UHS_4	95.4	Abundant	Melted	Melted	Not Melted
UHS_5	94.5	Marginal on the edge	Melted	Melted	Not Melted

To detect the phase produced during UHS and conventional sintering, diffractometric analyses were directly carried out on the sintered pellets; the corresponding patterns are shown in **Figure 3a**. The diffraction pattern of the powders calcined at 750°C for 1 h shows few really broad peaks all associated with a fluorite structure and indicating a poorly crystallized phase; the broadness of the peaks can also mask the presence of an amorphous phase and/or other minor crystalline phases. The sample Conv_1550 shows a single-phase fluorite-like structure (referred to CeO_2 - ICDD card n. 034-0394), as expected based on "standard deviation predictor" [29] and considered the sintering conditions. Secondly, all other samples, with the exception of UHS_1, also exhibit a single-phase fluorite-like structure; UHS_1 specimen is a multiphase material including a small amount of a secondary phase. The identification of the minor phase(s) is really difficult due to the very low intensity of the peaks which interferes with the detection limits of XRD and the probable overlapping to the peaks of fluorite. Anyway, the presence of some Bixbyite appears likely according to published results [46] (see the peaks marked with "B" in **Figure S2**). The other peaks, marked with Z and H in **Figure S2**, could be tentatively assigned to ZrO_2 (either tetragonal or cubic), and hexagonal Ln_2O_3, respectively. Finally, the lattice parameter of UHS samples (0.5426-0.5430 nm) is very similar to that of conventionally sintered (0.5432 nm) $Ce_{0.2}Zr_{0.2}Y_{0.2}Gd_{0.2}La_{0.2}O_{2-\delta}$, although some small differences can be detected. In particular, the cell in UHS samples appears slightly smaller and this might be related to the different treating atmosphere (reducing in UHS *vs.* oxidizing in conventional sintering) or to the different cooling rates (for instance, rapid cooling upon UHS might have quenched the high-temperature defect chemistry). Further investigations are needed to provide a detailed understanding of the lattice parameter evolution during UHS.
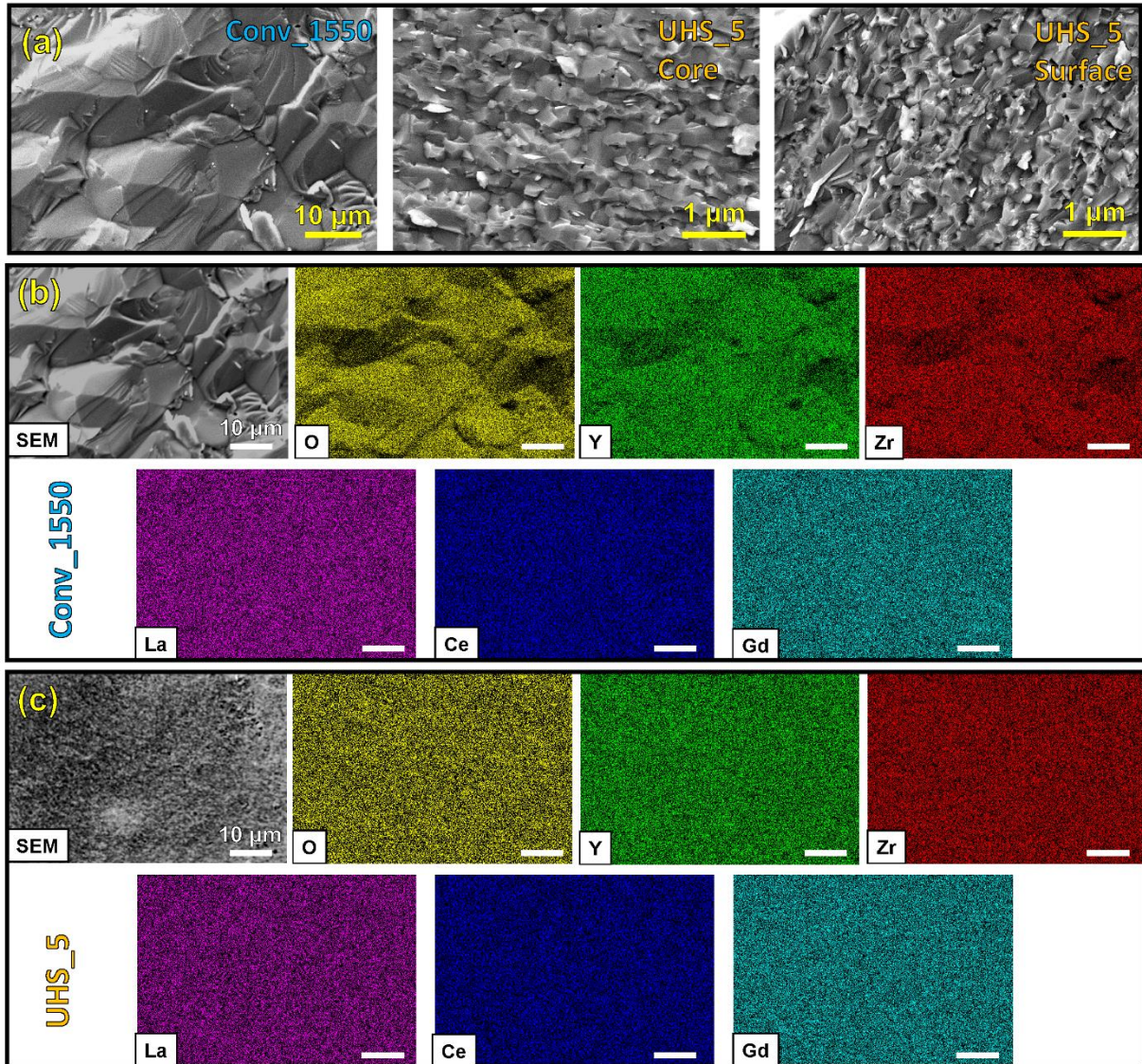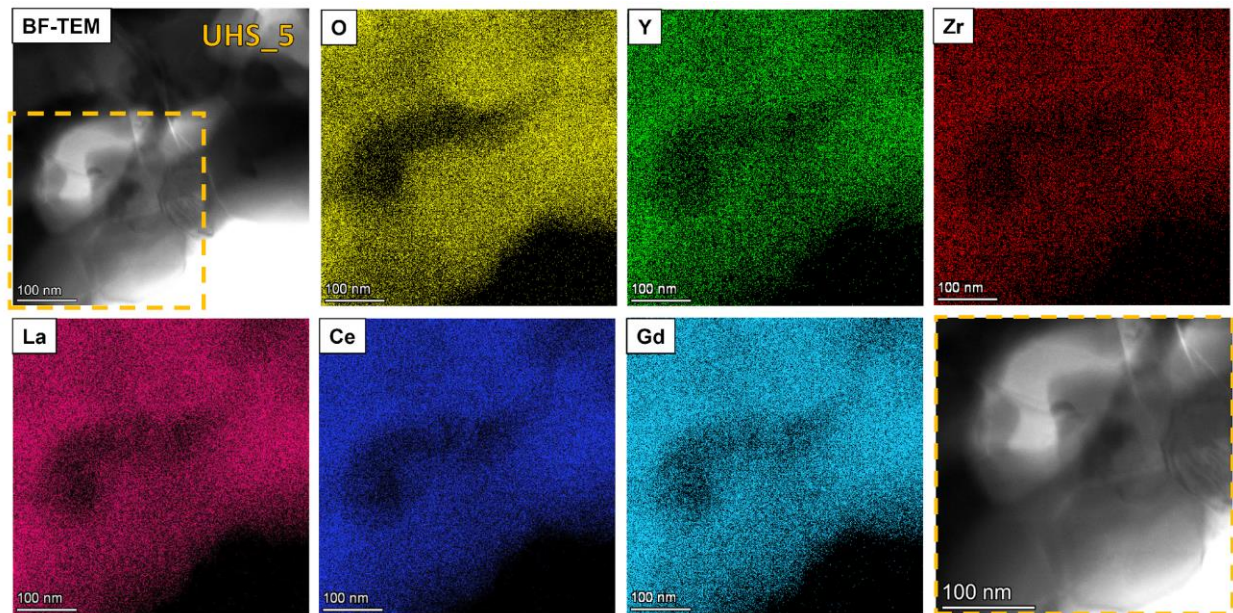
Figure 2. (a) SEM micrograph, and (b,c) EDXS elemental maps of conventionally sintered (1550°C, 2h) and UHS_5 samples. All pictures refer to fracture surfaces. The small variations in the light element EDXS counts in (b) can be attributed to the surface topology.

Despite its shortness, optimized UHS treatment appears very effective in obtaining densified pellets of $Ce_{0.2}Zr_{0.2}Y_{0.2}Gd_{0.2}La_{0.2}O_{2-\delta}$ (chosen as representative of Fluorite-structured Entropy-Stabilized Oxides - F-ESOs) stabilized in a single-phase fluorite-like crystal structure. ~~In addition to~~ Other than the beneficial effect on sintering, the present findings point out that UHS allows reaching the chemical equilibrium very quickly, even in complex ceramic systems manufactured by wet-chemical synthesis. This might be related to the fast heating path through the low-temperature region (<1150°C) where phase separation takes place (the starting material is

chemically homogeneous as precipitated from solution), thus facilitating the synthesis and sintering of single-phase materials. The presence of a secondary phase in the UHS_1 sample can be easily explained ~~if one considers~~ by considering the lower processing temperature which remains likely below (or just above) the threshold temperature for the single-phase stabilization (between 1100 and 1200 °C [29]).

The EDXS characterization results of the optimized UHS specimen reveal a highly homogeneous distribution of all cations both at the micron (**Figure 2**, SEM) and sub-micron (**Figure 3**, STEM) scale further confirming the XRD results which indicate the presence of an entropy-stabilized single-phase fluorite-like structure. Moreover, the TEM micrograph points out the presence of small grains thus proving that UHS is very effective to obtain dense and fine grained microstructures.


Figure 3. BF-TEM micrograph and EDXS elemental maps acquired in STEM mode on UHS_5 sample. Only topological variations of the EDXS counts can be detected. The micrograph on the right bottom corner reports a magnification of the same image highlighting the presence of small grain (≈ 150 nm).

The comparison between the Raman spectra of Conv_1550 and UHS_5 samples is reported in **Figure 4b**. The two materials show similar Raman features providing an additional confirmation that UHS allows obtaining ~~to obtain~~, in extremely short times, structural features analogous to that obtained in conventional processes. It is worth mentioning that Raman is very sensitive to short-range order, thus being substantially complementary to XRD (long-range order) and proving the

material purity at a smaller scale. Moreover, being each spectrum the result of the average of about 20 spectra acquired on different points of the pellets, the homogeneity of the material structure is assessed.

The Raman spectra show the typical CeO_2 band corresponding to the F_{2g} Raman mode from the space group Fm3m of cubic fluorite structure and attributed to symmetric breathing of mode of the O atoms around each cation[50]. The peak is however shifted to lower frequencies (centered at 440 cm^{-1}) due to the crystal lattice expansion of CeO_2 because of the introduction of larger ionic dopants [51](La^{3+} and Gd^{3+} have an ionic radius larger than Ce^{4+}) and the increasing number of oxygen vacancies. In particular, the vibrational modes at about 530 cm^{-1} and 630 cm^{-1}, are assigned to extrinsic and intrinsic oxygen vacancies, respectively [52], being the former due to the charge compensation arising from the substitution of Ce^{4+} ions by lower oxidation number ions and the latter to Ce^{3+} ions. This last mode appears slightly asymmetric thus suggesting that a second component at a higher frequency (645 cm^{-1}) can be singled out and ascribable to cubic Zr^{4+} in the fluorite structure [53,54]. The other two bands, at 287 and 358 cm^{-1}, are related to YSZ, as reported in the literature [53], thus suggesting that the presence of Zr^{4+} and Y^{3+} ions generates a further increase of the lattice disorder in fluorite structure. Finally, Raman characterization gives evidence of the high number of oxygen vacancies induced by the presence of a high number of cations ~~that substitute~~ substituting M^{4+} in the fluorite lattice positions.

Samples UHS_0, 2-5 showed an evident blackening on the external surfaces not influencing the diffraction pattern. This could be either attributed to a partial reduction of the specimens (UHS is carried out in Ar within C felts) or the carbon contamination from the felts. To identify the origin of such chromatic alterations (conventionally sintered samples were always yellowish), a TGA analysis was carried out in air on sample UHS_5. The thermogravimetric plot (**Figure 4c**) reveals a really small but clear increase of mass (around 0.25 %) in the range 300°C – 700°C. On the other hand, the conventionally sintered sample does not show any substantial mass variation in TGA. The weight gain after UHS can be attributed to the absorption of molecular oxygen from the atmosphere due to the oxidation of some Ce^{3+} (previously formed during UHS) according to the following defect reaction:

$$2Ce'_{Ce} + \frac{1}{2}O_{2(g)} + V_O^{\cdot\cdot} \rightarrow 2Ce_{Ce}^{x} + O_O^{x} \qquad (2)$$
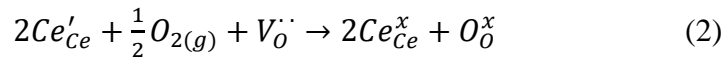
One can observe that if the blackening was related to carbon contamination, this would have resulted in a weight loss upon heating in air (which was not observed).
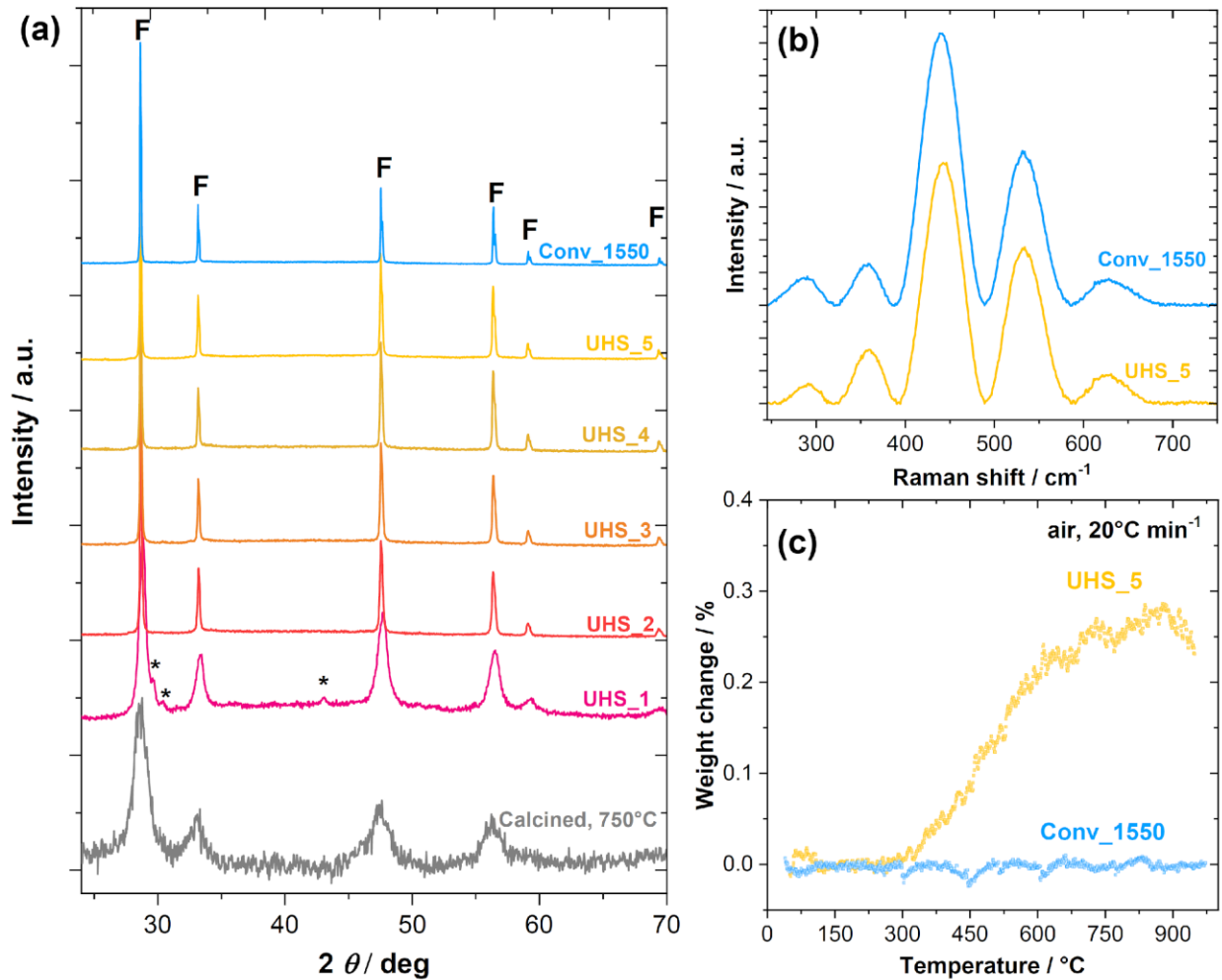
Figure 4. (a) XRD pattern of the calcined powder, UHS, and conventionally sintered samples; (b) Raman scattering spectra of conventionally sintered and UHS_5 samples; (c) TGA analysis (air, 20°C min^{-1}) of UHS_5 samples. Fluorite is labeled as "F", the secondary phases as "*".

~~In summary~~ Definitely, highly reactive powders of $Ce_{0.2}Zr_{0.2}Y_{0.2}Gd_{0.2}La_{0.2}O_{2-\delta}$ (chosen as representative of Fluorite-structured Entropy-Stabilized Oxides - F-ESO), prepared by using a simple and low-cost co-precipitation-based synthesis route, were sintered for the first time by UHS.

By optimizing the UHS cycle (in terms of applied current and exposure time) it was possible to obtain, in just about 2 min, nearly fully dense high-entropy ceramics completely converted and stabilized in a single-phase fluorite-like structure. Raman spectroscopy revealed the remarkable similarity between the UHS sample and the conventionally sintered one. Furthermore, the UHS specimens maintained their original nanometric features, owing to a perfectly homogeneous grain structure with grains whose size is in the order of a few hundreds of nanometers.

Acknowledgments

## References

[1]   M. Biesuz, S. Grasso, V.M. Sglavo, Curr. Opin. Solid State Mater. Sci. 24 (2020) 100868.

[2]   S. Grasso, Y. Sakka, G. Maizza, Sci. Technol. Adv. Mater. 10 (2009) 53001.

[3]   M. Bram, A.M. Laptev, T.P. Mishra, K. Nur, M. Kindelmann, M. Ihrig, J.G. Pereira da Silva, R. Steinert, H.P. Buchkremer, A. Litnovsky, F. Klein, J. Gonzalez-Julian, O. Guillon, Adv. Eng. Mater. 22 (2020).

[4]   J.D. Katz, Annu. Rev. Mater. Sci. 22 (1992) 153–170.

[5]   K.I. Rybakov, E.A. Olevsky, E. V. Krikun, J. Am. Ceram. Soc. 96 (2013) 1003–1020.

[6]   M. Cologna, B. Rashkova, R. Raj, J. Am. Ceram. Soc. 93 (2010) 3556–3559.

[7]   M. Biesuz, V.M. Sglavo, J. Eur. Ceram. Soc. 39 (2019) 115–143.

[8]   L. Spiridigliozzi, L. Pinter, M. Biesuz, G. Dell'Agli, G. Accardo, V.M. Sglavo, Materials (Basel). 12 (8), 1218.

[9]   V. Esposito, E. Traversa, J. Am. Ceram. Soc. 91 (2008) 1037–1051.

[10] M. Biesuz, L. Spiridigliozzi, M. Frasnelli, G. Dell'Agli, V.M. Sglavo, Mater. Lett. 190 (2017) 17–19.

[11] C. Wang, W. Ping, Q. Bai, H. Cui, R. Hensleigh, R. Wang, A.H. Brozena, Z. Xu, J. Dai, Y. Pei, C. Zheng, G. Pastel, J. Gao, X. Wang, H. Wang, J.-C. Zhao, B. Yang, X. (Rayne) Zheng, J. Luo, Y. Mo, B. Dunn, L. Hu, Science (80-.). 368 (2020) 521–526.

[12] M. Kermani, J. Dong, M. Biesuz, Y. Linx, H. Deng, V.M. Sglavo, M.J. Reece, C. Hu, S. Grasso, J. Eur. Ceram. Soc. 41 (2021) 6626–6633.

[13] J. Dong, V. Pouchly, M. Biesuz, V. Tyrpekl, M. Vilémová, M. Kermani, M. Reece, C. Hu, S. Grasso, Scr. Mater. 203 (2021) 114076.

[14] M. Biesuz, A. Galotta, A. Motta, M. Kermani, S. Grasso, J. Vontorová, V. Tyrpekl, M. Vilémová, V.M. Sglavo, Mater. Sci. Eng. C 127 (2021) 112246.

[15] R.-F. Guo, H.-R. Mao, Z.-T. Zhao, P. Shen, Scr. Mater. 193 (2021) 103–107.

[16] M. Ihrig, T.P. Mishra, W.S. Scheld, G. Häuschen, W. Rheinheimer, M. Bram, M. Finsterbusch, O. Guillon, J. Eur. Ceram. Soc. 41 (2021) 6075–6079.

[17]   R.-X. Luo, M. Kermani, Z.-L. Guo, J. Dong, C.-F. Hu, F. Zuo, S. Grasso, B.-B. Jiang, G.-L. Nie, Z.-Q. Yan, Q. Wang, Y.-L. Gan, F.-P. He, H.-T. Lin, J. Eur. Ceram. Soc. 41 (2021) 6338–6345.

[18]   J. Wu, Y. Lin, M. Kermani, C. Hu, S. Grasso, Ceram. Int. (2021).

[19]   M.N. Rahaman, Ceramic Processing and Sintering, Marcel Dekker, New York, USA, 1996.

[20]   M. Biesuz, G. Dell'Agli, L. Spiridigliozzi, C. Ferone, V.M.M. Sglavo, Ceram. Int. 42 (2016) 11766–11771.

[21]   C. Rost, Entropy-Stabilized Oxides: Explorations of a Novel Class of Multicomponent Materials, North Carolina State University, 2016.

[22]   C. Oses, C. Toher, S. Curtarolo, Nat. Rev. Mater. 5 (2020) 295–309.

[23]   E. Castle, T. Csanádi, S. Grasso, J. Dusza, M. Reece, Sci. Rep. 8 (2018) 8609.

[24]   J. Gild, Y. Zhang, T. Harrington, S. Jiang, T. Hu, M.C. Quinn, W.M. Mellor, N. Zhou, K. Vecchio, J. Luo, Sci. Rep. 6 (2016) 37946.

[25]   K. Chen, X. Pei, L. Tang, H. Cheng, Z. Li, C. Li, X. Zhang, L. An, J. Eur. Ceram. Soc. 38 (2018) 4161–4164.

[26]   K. Wang, B. Ma, T. Li, C. Xie, Z. Sun, D. Liu, J. Liu, L. An, Ceram. Int. 46 (2020) 18358–18361.

[27]   J. Dąbrowa, M. Stygar, A. Mikuła, A. Knapik, K. Mroczka, W. Tejchman, M. Danielewski, M. Martin, Mater. Lett. 216 (2018) 32–36.

[28]   M. Biesuz, S. Fu, J. Dong, A. Jiang, D. Ke, Q. Xu, D. Zhu, M. Bortolotti, M.J. Reece, C. Hu, S. Grasso, J. Asian Ceram. Soc. 7 (2019) 127–132.

[29]   L. Spiridigliozzi, C. Ferone, R. Cioffi, G. Dell'Agli, Acta Mater. 202 (2021) 181–189.

[30]   J. Gild, M. Samiee, J.L. Braun, T. Harrington, H. Vega, P.E. Hopkins, K. Vecchio, J. Luo, J. Eur. Ceram. Soc. 38 (2018) 3578–3584.

[31]   P. Malinovskis, S. Fritze, L. Riekehr, L. Von Fieandt, J. Cedervall, D. Rehnlund, L. Nyholm, E. Lewin, U. Jansson, Mater. Des. 149 (2018) 51–62.

[32]   Y.-W. Chen, J.-J. Ruan, J.-M. Ting, Y.-H. Su, K.-S. Chang, Ceram. Int. 47 (2021) 11451–11458.

[33]   F. Wang, X. Yan, T. Wang, Y. Wu, L. Shao, M. Nastasi, Y. Lu, B. Cui, Acta Mater. 195 (2020) 739–749.

[34]   A. Mao, H.-Z. Xiang, Z.-G. Zhang, K. Kuramoto, H. Yu, S. Ran, J. Magn. Magn. Mater. 484 (2019) 245–252.

[35]   D. Bérardan, S. Franger, D. Dragoe, A.K. Meena, N. Dragoe, Phys. Status Solidi - Rapid Res. Lett. 10 (2016) 328–333.

[36]   D. Bérardan, S. Franger, A.K. Meena, N. Dragoe, J. Mater. Chem. A 4 (2016) 9536–9541.

[37] A. Salian, S. Mandal, Crit. Rev. Solid State Mater. Sci. (2021) 1–52.

[38] A. Sarkar, L. Velasco, D. Wang, Q. Wang, G. Talasila, L. de Biasi, C. Kübel, T. Brezesinski, S.S. Bhattacharya, H. Hahn, B. Breitung, Nat. Commun. 9 (2018) 3400.

[39] A. Sarkar, Q. Wang, A. Schiele, M.R. Chellali, S.S. Bhattacharya, D. Wang, T. Brezesinski, H. Hahn, L. Velasco, B. Breitung, Adv. Mater. 31 (2019) 1806236.

[40] R. Zhang, M.J. Reece, J. Mater. Chem. A 7 (2019) 22148–22162.

[41] A. Amiri, R. Shahbazian-Yassar, J. Mater. Chem. A 9 (2021) 782–823.

[42] M. Zhang, X. Xu, Y. Yue, M. Palma, M.J. Reece, H. Yan, Mater. Des. 200 (2021) 109447.

[43] H. Chen, J. Fu, P. Zhang, H. Peng, C.W. Abney, K. Jie, X. Liu, M. Chi, S. Dai, J. Mater. Chem. A 6 (2018) 11129–11133.

[44] Z.-W. Huang, K.-S. Chang, Ceram. Int. 47 (2021) 22558–22566.

[45] L. Xu, H. Wang, L. Su, D. Lu, K. Peng, H. Gao, J. Eur. Ceram. Soc. 41 (2021) 6670–6676.

[46] L. Spiridigliozzi, C. Ferone, R. Cioffi, G. Accardo, D. Frattini, G. Dell'Agli, Materials (Basel). 13 (2020) 558.

[47] W. Ji, J. Zhang, W. Wang, Z. Fu, R.I. Todd, J. Eur. Ceram. Soc. 40 (2020) 5829–5836.

[48] W. Ji, B. Parker, S. Falco, J.Y. Zhang, Z.Y. Fu, R.I. Todd, J. Eur. Ceram. Soc. 37 (2017) 2547–2551.

[49] L.A. Perez-Maqueda, E. Gil-Gonzalez, A. Perejon, J.-M. Lebrun, P. Sanchez-Jimeneza, R. Raj, J. Am. Ceram. Soc. 100 (2017) 3365–3369.

[50] J.R. McBride, K.C. Hass, B.D. Poindexter, W.H. Weber, J. Appl. Phys. 76 (1994) 2435–2441.

[51] M.J. Kishor Kumar, J.T. Kalathi, J. Alloys Compd. 748 (2018) 348–354.

[52] S.A. Acharya, V.M. Gaikwad, V. Sathe, S.K. Kulkarni, Appl. Phys. Lett. 104 (2014) 113508.

[53] I. Kosacki, V. Petrovsky, H.U. Anderson, P. Colomban, J. Am. Ceram. Soc. 85 (2004) 2646–2650.

[54] S.N. Basahel, T.T. Ali, M. Mokhtar, K. Narasimharao, Nanoscale Res. Lett. 10 (2015) 73.
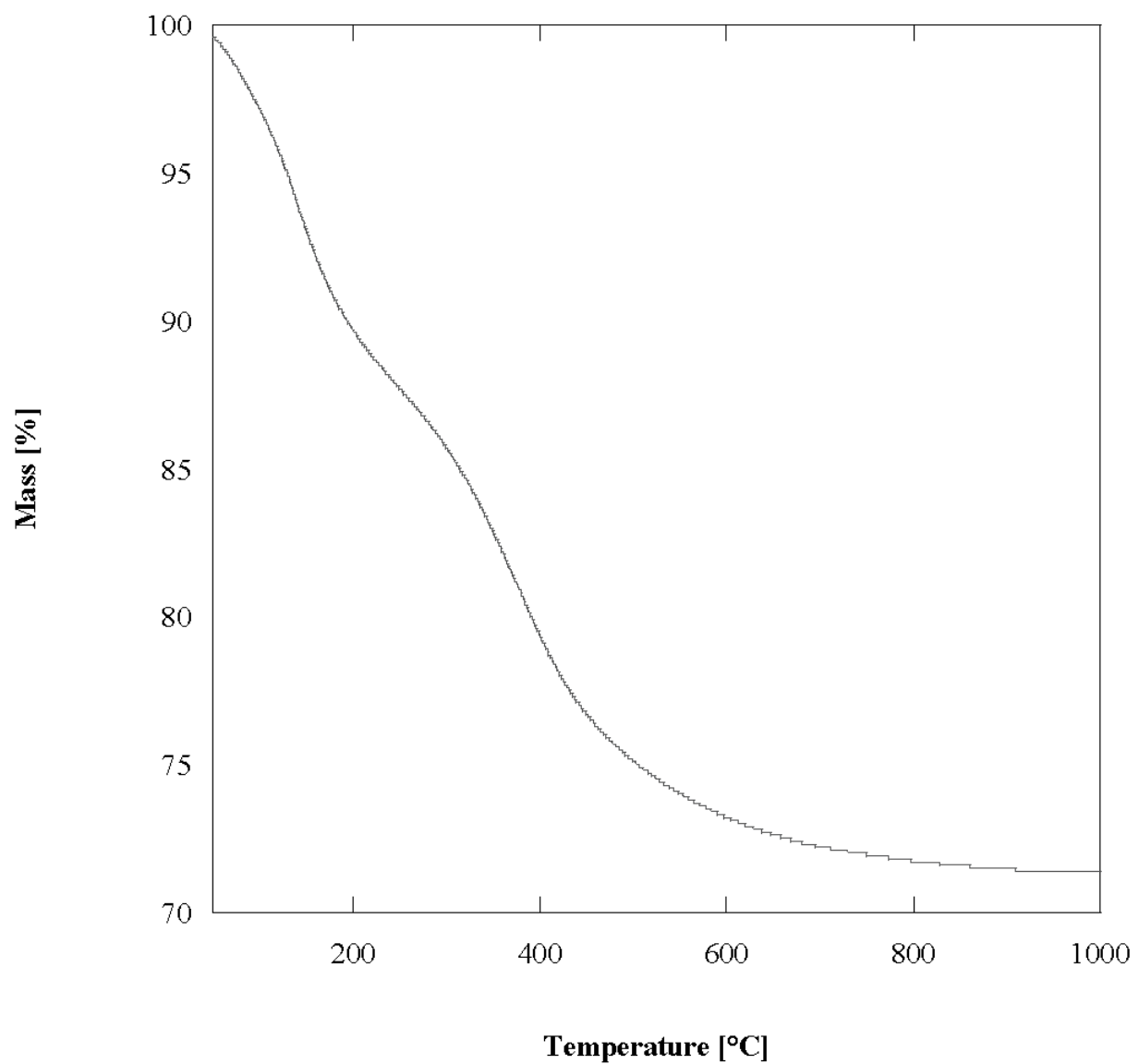
Figure S1. Thermogravimetric analysis of the as-synthesized $Ce_{0.2}Zr_{0.2}Y_{0.2}Gd_{0.2}La_{0.2}O_{2-\delta}$.
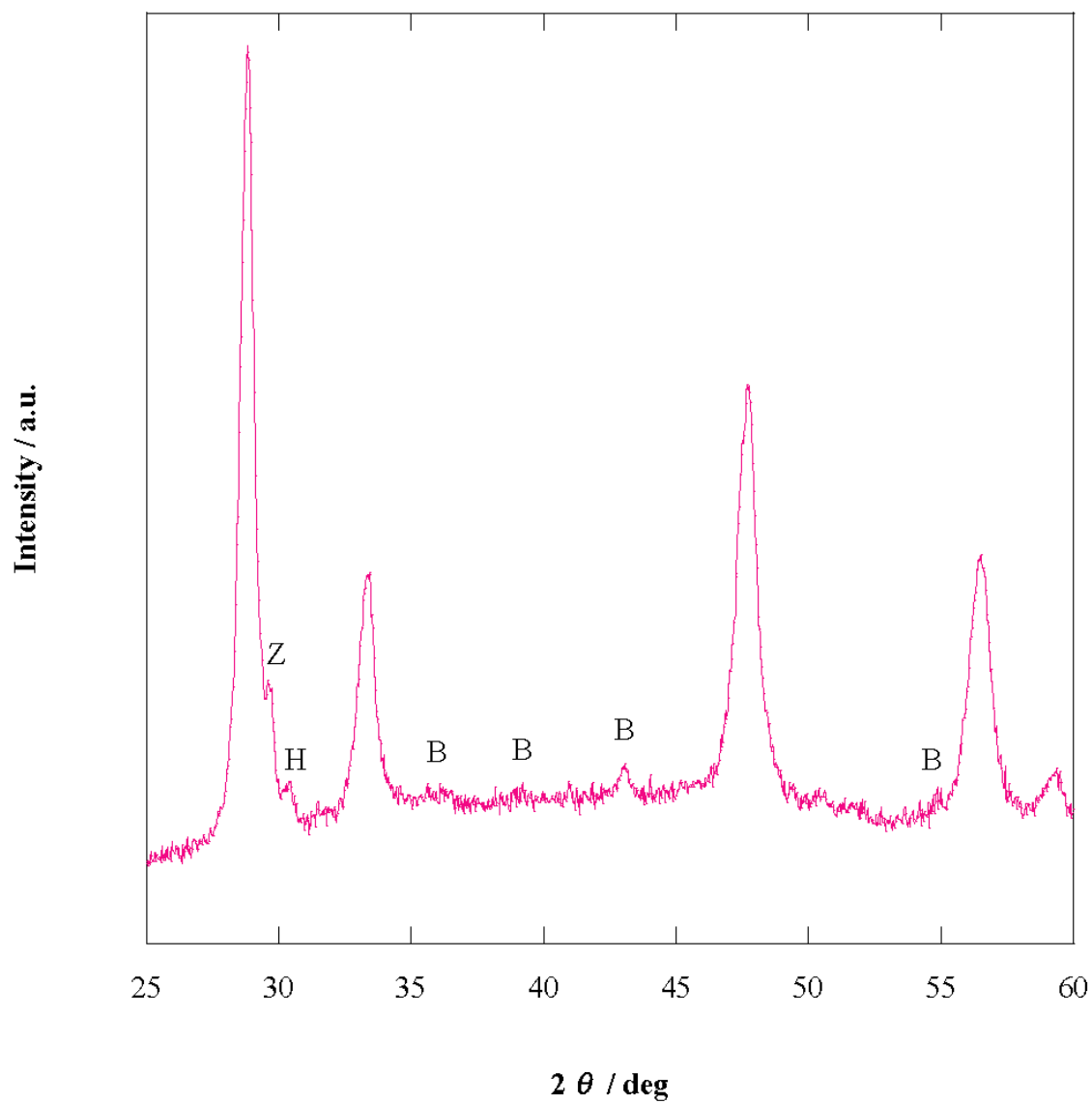
Figure S2. XRD pattern of sample UHS_1, highlighting the presence of several secondary phases (labeled as Z, H and B, respectively).